distribution is random, where some monomeric units may have more than one carboxylic group and other have none. The higher concentration and a more uniform distribution of the carboxylic groups along the chain in alginate (Fig. 1A) could be responsible for the better transport of Li ions in the vicinity of Si particles, more uniform coverage, and more efficient assistance in the formation of a stable SEI layer on the Si surface (Fig. 4). Alginate macromolecules are also much more polar than the CMC polymer chains, which can ensure better interfacial interaction between the polymer binder and the particles, as well as stronger adhesion between the electrode layer and Cu substrate. This large difference in chemistry of CMC and alginate results in major differences in their behavior. For example, the alginate solution in water has dramatically higher viscosity than CMC (fig. S7). This high viscosity prevents Si particles from sedimentation and aggregation during the electrode formation, as water is evaporating, resulting in high slurry uniformity. This uniformity is known to be critical for obtaining uniform distribution of active materials within the anode needed for the long-term electrode stability. Alginate solution also exhibits a much higher degree of shear-thinning behavior (fig. S8), which offers an opportunity to lower a slurry viscosity needed for fast homogenization by increasing the mixing rate and an opportunity to increase a slurry viscosity for porosity and uniformity control during the electrode formation by lowering the mixing rate. To achieve viscosity comparable to alginate solutions, substantially higher CMC content is needed. Similarly, to get a remotely comparable performance with a CMC binder, one needs to increase the binder:Si ratio by a factor of 4 (*1*, *13*). The high binder content decreases the electrical conductivity of the electrode and necessitates the use of a higher content of the conductive carbon additives (increasing the C:Si ratio by a factor of 3) (*1*), which inevitably lowers the electrode specific capacity.

To further characterize the behavior of the alginate-based electrode, we performed cyclic voltammetry experiments. The differential capacity curves show one broad Li insertion (cathodic) peak at ~0.21 V and two Li extraction (anodic) peaks at 0.33 and 0.51 V (Fig. 3D). The origin of the potential difference between the corresponding peaks in the cathodic and anodic directions is commonly modeled by a thermodynamic (rate-independent) hysteresis (*30*). The first 0.33-V anodic peak is not always observed. In some Si-C nanocomposite particles, for example, only one Li extraction peak at ~0.5 V appears (*6*). Therefore, the 0.33-V peak could be related to the surface properties of Si. A small Li-extraction peak observed at ~0.17 V corresponds to Li deintercalation from C additives. The five cyclic voltammetry cycles (Fig. 3D) demonstrate high reproducibility, indicative of good anode stability.

The shapes of the galvanostatic Li insertion and extraction profiles for the produced Si anodes (Fig. 3C and fig. S4B) are similar to the profiles previously reported in literature for other Si electrodes (*6*, *9*, *13*). In contrast to intercalation-type electrode materials, these profiles do not exhibit strictly horizontal plateaus and cover a larger potential range. The Li-extraction profiles become more horizontal and exhibit slightly smaller overpotential with cycling (fig. S4B), suggesting a gradual improvement in the discharge kinetics (*20*). The current-dependent overpotential increases the Li-extraction potential when current density is increased from 140 to 4200 mA/g (*20*) (Fig. 3C). By comparing the Li-extraction capacities achieved at different current densities (Fig. 3C), we can conclude that these electrodes possess moderate rate capability, inferior to that achieved in Si-C composite anodes with hierarchical porosity (*6*) or in nanowires (*5*, *10*). The advantage of this traditional battery technology, however, is higher volumetric capacity, higher CE, and compatibility with existing manufacturing techniques. Further electrode optimization and introduction of additional pores is expected to substantially increase the rate performance, because the diffusion of Li into or out of Si nanoparticles can be achieved within minutes (*20*).

In addition to improving performance of Si anodes, the alginate properties may provide advantages to other electrodes, such as traditional graphitic anodes. For example, replacing PVDF with lower-cost, environmentally friendly alginate was found to improve the first-cycle CE and cycle stability (fig. S5).

References and Notes

1. J. S. Bridel, T. Azais, M. Morcrette, J. M. Tarascon, D. Larcher, *Chem. Mater.* **22**, 1229 (2010).
2. L. Fransson, T. Eriksson, K. Edstrom, T. Gustafsson, J. O. Thomas, *J. Power Sources* **101**, 1 (2001).
3. S. S. Zhang, T. R. Jow, *J. Power Sources* **109**, 422 (2002).
4. D. Guy, B. Lestriez, D. Guyomard, *Adv. Mater.* **16**, 553 (2004).
5. C. K. Chan *et al.*, *Nat. Nanotechnol.* **3**, 31 (2008).
6. A. Magasinski *et al.*, *Nat. Mater.* **9**, 353 (2010).
7. K. Kang *et al.*, *Appl. Phys. Lett.* **96**, 053110 (2010).
8. B. Hertzberg, A. Alexeev, G. Yushin, *J. Am. Chem. Soc.* **132**, 8548 (2010).
9. D. Mazouzi, B. Lestriez, L. Roue, D. Guyomard, *Electrochem. Solid-State Lett.* **12**, A215 (2009).
10. H. Kim, J. Cho, *Nano Lett.* **8**, 3688 (2008).
11. M. H. Park *et al.*, *Nano Lett.* **9**, 3844 (2009).
12. A. Magasinski *et al.*, *ACS Appl. Mater. Interfaces* **2**, 3004 (2010).
13. S. D. Beattie, D. Larcher, M. Morcrette, B. Simon, J. M. Tarascon, *J. Electrochem. Soc.* **155**, A158 (2008).
14. O. Smidsrod, K. I. Draget, *Carbohydr. Eur.* **14**, 6 (1996).
15. A. J. de Kerchove, M. Elimelech, *Biomacromolecules* **8**, 113 (2007).
16. K. I. Draget, G. Skjåk-Braek, O. Smidsrød, *Int. J. Biol. Macromol.* **21**, 47 (1997).
17. J. Li, R. B. Lewis, J. R. Dahn, *Electrochem. Solid-State Lett.* **10**, A17 (2007).
18. T. A. Fenoradosoa *et al.*, *J. Appl. Phycol.* **22**, 131 (2010).
19. S. K. Papageorgiou *et al.*, *Carbohydr. Res.* **345**, 469 (2010).
20. R. Chandrasekaran, A. Magasinski, G. Yushin, T. F. Fuller, *J. Electrochem. Soc.* **157**, A1139 (2010).
21. M. N. Obrovac, L. Christensen, *Electrochem. Solid-State Lett.* **7**, A93 (2004).
22. E. Peled, D. Golodnitsky, G. Ardel, V. Eshkenazy, *Electrochim. Acta* **40**, 2197 (1995).
23. D. Aurbach, *J. Power Sources* **89**, 206 (2000).
24. J. B. Goodenough, Y. Kim, *Chem. Mater.* **22**, 587 (2010).
25. Z. Gadjourova, Y. G. Andreev, D. P. Tunstall, P. G. Bruce, *Nature* **412**, 520 (2001).
26. S. Ohara, J. Suzuki, K. Sekine, T. Takamura, *J. Power Sources* **136**, 303 (2004).
27. J. W. Choi *et al.*, *Nano Lett.* **10**, 1409 (2010).
28. L. El Ouatani *et al.*, *J. Power Sources* **189**, 72 (2009).
29. J. C. Guo, C. S. Wang, *Chem. Commun.* **46**, 1428 (2010).
30. M. D. Levi, D. Aurbach, *J. Phys. Chem. B* **101**, 4630 (1997).

Acknowledgments: This work was partially supported by Georgia Institute of Technology, Honda Initiation Grant, Clemson Univ., and NASA grant NNX09CD29P. Patent application PCT US 113507 has been filed.

Supporting Online Material

www.sciencemag.org/cgi/content/full/science.1209150/DC1
Material and Methods
Figs. S1 to S9

31 May 2011; accepted 19 August 2011
Published online 8 September 2011;
10.1126/science.1209150

A Self-Quenched Defect Glass in a Colloid-Nematic Liquid Crystal Composite

T. A. Wood, J. S. Lintuvuori, A. B. Schofield, D. Marenduzzo, W. C. K. Poon*

Colloidal particles immersed in liquid crystals frustrate orientational order. This generates defect lines known as disclinations. At the core of these defects, the orientational order drops sharply. We have discovered a class of soft solids, with shear moduli up to 10^4 pascals, containing high concentrations of colloidal particles (volume fraction $\phi \gtrsim 20\%$) directly dispersed into a nematic liquid crystal. Confocal microscopy and computer simulations show that the mechanical strength derives from a percolated network of defect lines entangled with the particles in three dimensions. Such a "self-quenched glass" of defect lines and particles can be considered a self-organized analog of the "vortex glass" state in type II superconductors.

In a typical colloidal suspension, particles are dispersed in a simple, isotropic liquid that acts as a passive, homogeneous background medium. But it is also possible to disperse particles in a liquid that itself has complex properties. For example, particles in a demixing binary

liquid mixture may gather at and arrest the bicontinuous interface separating the two phases (*1*). Another class of dispersions with complex suspending media is particles in liquid crystals (LCs) (*2*, *3*), in which upon cooling, the dispersing medium can undergo a succession of phase transitions from an isotropic liquid to a nematic or other ordered mesophase (*4*). The competition between ordering in the bulk of a mesophase and on the surface of particles gives rise to the possibility of new microstructures and functions, e.g., as biosensors (*5*, *6*), but also to barriers against dispersing the particles in the first place. The latter feature means that, to date, there have been few successful attempts at dispersing high concentrations of particles into LCs. But analogy with dispersions in simple liquids suggests that constructing a colloid-LC composite at high particle volume fraction, ϕ, may pay rich dividends both in terms of applications (for instance, better mechanical stability) and fundamental science (for example, understanding glassy arrest).

We have synthesized a soft solid (Fig. 1) by dispersing a high concentration ($\phi \leq 50\%$) of particles directly into a nematic LC. This contrasts with the majority of previous work where $\phi \to 0$, and the particles were initially dispersed into the isotropic phase. Computer simulations show that the rigidity (Fig. 2) of our new colloid-LC gel (Fig. 3) is due to particle-entangled defect lines percolating in three dimensions (Fig. 4). Rigidity is important because LCs are increasingly being used as biomedical sensors (*7*), for which materials able to support their own weight (*5*) and the weight of embedded living cells (*6*) are needed. Our findings are also of fundamental interest to a larger audience interested in interacting line defects, from LCs in porous media (*8*) through vortices in superconductors (*9*) to cosmic strings (*10*).

In a (thermotropic) nematic LC, the anisotropic molecules align, on average, along a director, **n**. The physics of single particles in nematic LCs is reasonably well known in broad outline only in the $\phi \to 0$ limit (*11*). A particle (radius a) anchors the LC molecules to its surface, either in parallel or perpendicularly (homeotropic), with energy $\sim Wa^2$ (where W is the anchoring strength), giving rise to an inhomogeneous director field $\mathbf{n}(\mathbf{r})$ and stored elastic energy $\sim Ka$ (where K is an average Frank elastic constant). For weak anchoring, $Wa/K \ll 1$, $\mathbf{n}(\mathbf{r})$ is continuous. As Wa/K increases, topological singularities appear: first, an equatorial ring on the particle surface, and then a ring away from the surface (a "Saturn ring"), either of which generates an $\mathbf{n}(\mathbf{r})$ with quadrupolar symmetry. But at the highest value of Wa/K, a defect pattern with a totally different (dipolar) symmetry appears.

Although the conditions under which these defects occur are still open to debate (*12*), it is clear that the elastic distortion associated with any of these defects around a particle induces an anisotropic interparticle attraction. In a confined, two-dimensional (2D) environment where the nematic LC is aligned parallel to the confining planes (a 2D planar nematic cell), such elasticity-mediated interparticle interaction gives rise to straight chains (for dipoles) (*2*) and zigzag lines (for Saturn rings) (*13*) when ϕ is vanishingly small ($\phi \to 0$). In these multiparticle structures, the defect around each particle retains its individual character. Recent simulations and experiments (*14*–*16*) have revealed that multiparticle structures can also form when particle-mediated defects become entangled. Again, in a 2D planar nematic cell, different entangled-defect configurations around particles can give rise to various multiparticle clusters (chains, etc.), as well as 2D crystals (*13*). A simulation study (*15*) of 3D self-assembly of particles in a nematic LC at finite ϕ ($\lesssim 8\%$) showed a more or less random dispersion of planar clusters.

Experimental study of such defect-mediated colloidal self-assembly is challenging for kinetic reasons. The calculated phase diagram of a colloid-LC mixture (*17*) shows that below the isotropic-nematic transition temperature (T_{IN}), a practically particle-free nematic phase should coexist with particles at $\phi \approx 64\%$. Thus, we expect all space-filling defect-mediated particle structures to be metastable. Simply quenching a particle-laden isotropic LC below T_{IN} in the bulk does not produce such structures. Instead, particles are swept along by fast nematic-isotropic fronts and

Scottish Universities Physics Alliance and School of Physics and Astronomy, The University of Edinburgh, James Clerk Maxwell Building, Kings Buildings, Mayfield Road, Edinburgh, EH9 3JZ, UK.

*To whom correspondence should be addressed. E-mail: w.poon@ed.ac.uk

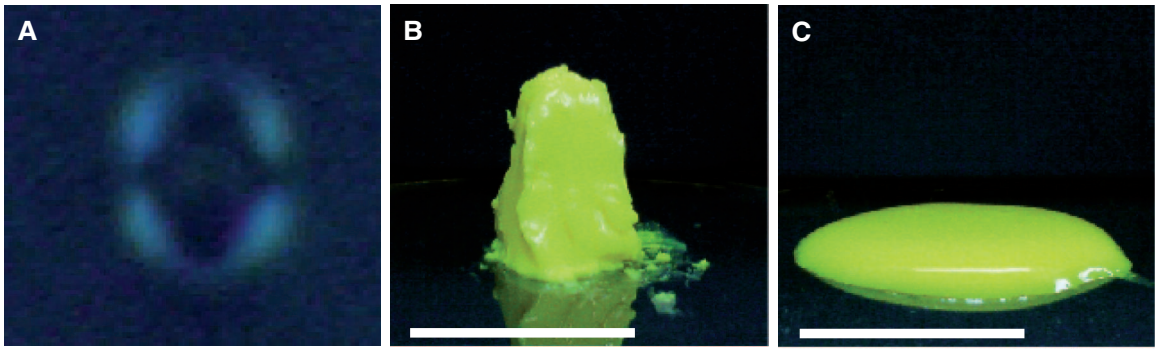

Fig. 1. (A) A quadrupolar birefringence pattern around a 2-μm-diameter particle in a uniformly aligned nematic cell. **(B)** A colloid-nematic composite at ϕ = 49% can be sculpted as a solid at room temperature. **(C)** The sculpture melts at the isotropic-nematic transition temperature. Scale bars, 1 cm.

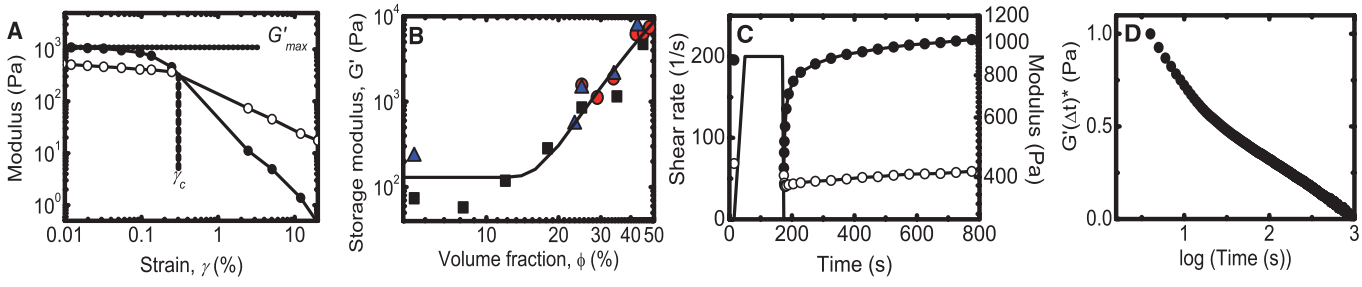

Fig. 2. (A) Measured storage (G', black circles) and loss (G'', open circles) moduli as a function of strain amplitude (γ) at ϕ = 28%. **(B)** Maximum storage modulus as a function of volume fraction ϕ. Particle diameters are 0.7 μm (black squares), 1.2 μm (red circles), and 2.0 μm (blue triangles); the line is a guide for the eye. **(C)** Storage and loss moduli measured before and after a ϕ = 28% sample is sheared at 200 s^{-1} for 150 s, with the shear history shown by the continuous line. **(D)** Plot of $G'(\Delta t)^* = [G'_{max} - G'(\Delta t)]/(G'_{max} - G'_0)$, versus the time elapsed (Δt) since the cessation of shear. Here, G'_{max} is the maximum modulus attained during our experimental period, and G'_0 is the modulus at $\Delta t = 0$.

eventually become trapped between nematic domains, giving rise to a cellular solid (*17*). (A bulk simulation that is smaller than the size of a typical nematic domain does not face this constraint.) In 2D experiments (*16*), well-defined boundary conditions (hence, the planar nematic cell) and local laser preheating are necessary to observe defect-entangled particle clusters.

We generated extended defect-mediated particle structures by dispersing sterically stabilized polymethylmethacrylate (PMMA) particles ($2a$ = 0.7, 1.2, 2 μm) directly into the bulk nematic phase of 4-cyanobiphenyl (5CB) (T_{IN} = 35.2°C) in untreated 2-cm^3 sample bottles at room temperature (≈19°C). (Note that, as in other similar systems (*17*), no measurable shift in T_{IN} due to particle dispersion was found.) The core of the particles includes the dye 7-nitrobenzo-2-oxa-1,3-diazolemethylmethacrylate chemically linked to the PMMA polymer. Polarized optical microscopy shows that single particles are surrounded by a quadrupolar director field (Fig. 1A), consistent with either a surface or Saturn-ring defect. From this, we estimate an upper bound for our anchoring strength: A quadrupolar director field should only occur if $Wa/K \lesssim 25$ for particles in 5CB (*11*).

Attempts to disperse dried PMMA particles into nematic 5CB by hand-shaking failed; large clumps of undispersed particles, presumably held together by entangled defects, sedimented. Our simulations suggest that it takes ~$10^2 k_B T$ (k_B, the Boltzmann constant; T, temperature) to break such clumps. We used vigorous mechanical agitation on a "whirly mixer" to input this energy and produce well-dispersed samples. We estimate that our shaking induces maximum velocities on the order of $v \sim 10^{-2}$ m s^{-1}, and the viscosity of 5CB at room temperature is $\eta \approx 20$ mPa s^{-1} (*18*), so that a typical force at the particle level is $F \sim \eta v a \sim 200$ pN. The work done by this force over a distance on the order of a disclination core, $l_c \sim 5$ nm (*19*), is $Fl_c \sim 200 k_B T$, consistent with our estimate of the energy barrier for dispersion.

Here, we focus on samples with $\phi \gtrsim 5\%$. Macroscopically, none of our samples sedimented over long times (up to many months); that is, particles remain dispersed throughout the whole volume of the LC. All samples were solid enough to be scooped out of their vials. Within the range $5\% \lesssim \phi \lesssim 20\%$, samples had a "curdlike" appearance. As ϕ increased above 8%, larger aggregates became visible within the curdlike sample, and the aggregate size increased with volume fraction until the samples adopted a homogeneous appearance at $\phi \approx 23\%$. At the highest concentrations reached, $\phi \gtrsim 50\%$, samples were found to be highly malleable. A sculpture molded by a metal spatula is shown in Fig. 1B. When heated to above T_{IN}, this sculpture melted into a liquid (Fig. 1C), demonstrating that the rigidity is provided by the nematic order.

We probed the mechanical properties of these arrested states using oscillatory rheometry in a cone-plate stress-controlled rheometer (TA Instruments, New Castle, DE, AR2000; 40 mm, 1° cone) at a frequency of 1 Hz. The cone and plate presented rough boundary conditions and homeotropic anchoring to the LC molecules. All samples with $\phi \gtrsim 5\%$ exhibited solidlike responses at low strain amplitudes (γ) with plateaus in both the storage (G') and loss (G'') moduli that are γ-independent. The plateau moduli satisfy $G''_{max}/G'_{max} \lesssim 0.5$; the behavior of the sample shown in Fig. 2A is typical. At $\phi \lesssim 10\%$, the plateau storage modulus (G'_{max}) is essentially constant (Fig. 2B), staying at $G'_{max} = G_0 \lesssim 10^2$ Pa. Beyond $\phi \approx 10\%$, $G'_{max}(\phi)$ increases rapidly with ϕ, with a functional form that is consistent with $G'_{max}(\phi) - G_0 \sim (\phi - \phi_c)^\nu$ with $\nu = 2.5 \pm 0.5$ and $\phi_c = 0.12 \pm 0.01$; data for three different particle sizes collapse onto the same curve.

As the strain amplitude increases, both G' and G'' begin to drop, with the former dropping faster than the latter so that they eventually cross. Again, the behavior shown in Fig. 2A is typical. The crossing may be taken as the point at which a solidlike ($G' > G''$) colloid-nematic composite yields into a liquidlike state ($G' < G''$). It was difficult to obtain reliable values of the yield strain (γ_c) at low ϕ. Above $\phi \sim 0.1$, γ_c settles down to values well below 1% (Fig. 2A), reaching $\gamma_c \approx 0.2\%$ at $\phi \approx 60\%$.

We also used rheometry to probe the kinetics of network formation. We shear-melted the gel structure at a steady shear rate of 200 s^{-1}, then switched off the steady shear and monitored the recovery of G' and G'' as a function of time (Fig. 2C). Plotting $G'(t)$ against the logarithm of elapsed time since the cessation of shear (Fig. 2D) shows a two-staged recovery of solidlike behavior. Half of the recovery is fast, complete in ~10 s, then the process dramatically slows down, with the rest of the recovery not complete for another ~10^3 s. Both stages of the recovery, especially the much slower second stage, are linear in this representation.

The rheology data in Fig. 2B suggest that there are two regimes of gel behavior: below and above $\phi \approx 15\%$. To make sense of these two regimes, we turn to confocal microscopy (performed with the use of a Nikon TE300 inverted microscope and a BioRad Radiance 2100 scanner at an incident wavelength of 488 nm). The thickness of the sample was ~100 μm. Due to turbidity, we could only image ~10 μm into each sample. We show images typical of the two regimes, $5\% \lesssim \phi \lesssim 10\%$ and $\phi \gtrsim 20\%$, respectively. A sample at $\phi = 6\%$ shows disconnected clusters of particles (Fig. 3A). These clusters do not show any visible thermal fluctuations (Brownian motion). On the other hand, the sample at $\phi = 33\%$ shows a connected particle structure (Fig. 3B). This qualitative change in the microstructure presumably lies behind the change from approximately constant G' to a regime in which G' increases strongly with ϕ.

To understand this transition from single clusters to a space-filling network, we need to know how the defect lines interact with the particles. We performed extensive simulations of the behavior of defect lines interacting with multiple particles (radius a) in a 3D box of volume $(12a)^3$ with periodic boundary conditions [see supporting online material (SOM) for all algorithmic details]. We used a Landau-de Gennes model (*4*) at two anchoring strengths, $Wa/K \approx 15$ and 30, bracketing our estimate of the upper bound of the anchoring strength in our system $Wa/K \lesssim 25$. We also studied a range of finite particle volume fractions: $3\% < \phi < 30\%$. Particles move according to a molecular-dynamics algorithm defined on the basis of the elastic forces calculated by integrating the LC stress tensor over their surfaces. Thermal noise is also included, although elastic forces dominate. The LC order parameter relaxes to minimize the Landau-de Gennes free energy, which consists of: (i) a bulk term favoring nematic ordering in the bulk; (ii) a distortion term penalizing splay, twist, and bend deformations in $\mathbf{n}(\mathbf{r})$; and (iii) an anchoring energy that favors normal anchoring of $\mathbf{n}$ at the particle surface. The time scale of the relaxational dynamics is given by the rotational viscosity of the LC. We typically started simulations from an isotropic configuration quenched to the nematic phase. We identify defect lines as regions where the order parameter drops below 60% of its maximum bulk value.

The size of particle clusters that are entangled by a single defect line increases with ϕ. We

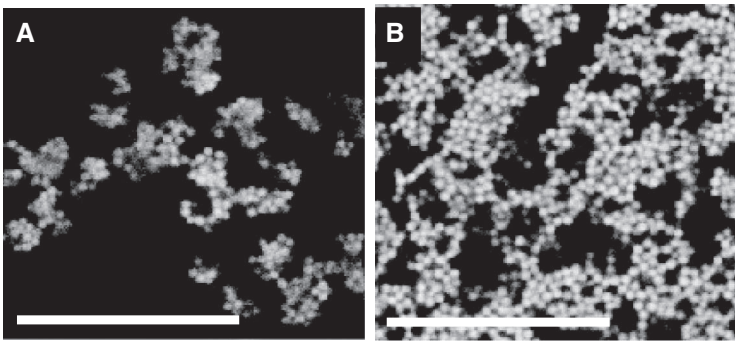

Fig. 3. (**A**) Confocal micrograph at $\phi = 6\%$: Colloids aggregate in loosely connected clusters within large expanses of a nematic LC. (**B**) At $\phi = 33\%$, the colloid structure is densely knitted around small nematic domains. Scale bars, 20 μm.

quantify this by plotting the volume of defect lines associated with the largest defect-entangled, system-spanning cluster (normalized by the total defect volume) as a function of ϕ (Fig. 4A). At low volume fractions, $\phi \lesssim 5\%$, we see some isolated particles supporting Saturn-ring defects. Even at such ϕ, the Saturn-ring defects on neighboring particles can already merge to form entangled point defects, giving rise to clusters of a few particles, some of which can be linear or planar (see Fig. 4B for an example). In the steady-state configuration, clusters interact and hold each other in place through long-range elastic distortions in the LC. This is confirmed by an inverse quench into the isotropic phase, which releases elastic forces and quickly leads to the dissolution of the clusters.

A fully percolated defect structure emerges at $\phi \approx 15$ to 20% (Fig. 4C, see also fig. S3 for versions with the particles removed). Interestingly, the volume fraction at which this occurs does not depend much on anchoring strength for the range we simulated. What is crucial is the nature of the anchoring: We find that entangled defect structures are not observed with planar anchoring of the LC at particle surfaces.

These simulations throw light on our bulk observations, rheological measurements, and microscopy images. First, our simulations allow us to estimate typical energy barriers between states. In particular, we find that an energy on the order of 10^2 to $10^3 k_B T$ is needed to form a dimer held together by a defect line starting from separated colloidal particles (see SOM). This is consistent with our earlier estimate of an input of $\gtrsim 10^2 k_B T$ in vigorous shaking to mix particles into nematic 5CB to prepare our samples.

Visually, both confocal microscopy and simulations find two aggregation regimes: isolated clusters (Figs. 3A and 4B) and space-spanning clusters (Figs. 3B and 4C). Our simulations suggest that these clusters are held together by entangled defects. In the simulations, the isolated clusters at low ϕ hold each other in place by the elastic interaction mediated by the LC, which we take to be the origins of the finite storage modulus, $G'_0 \sim 10^2$ Pa, in our samples at $\phi \lesssim 10\%$ (Fig. 2B). The curdlike appearance of our samples in the range $5\% \lesssim \phi \lesssim 20\%$ is presumably due to the presence of large clusters of this kind.

We associate the sharp change in rheological properties observed at $\phi \gtrsim 20\%$ (Fig. 2B) with the emergence of a system-spanning cluster held together by percolated defect lines seen in simulations at around the same particle concentration (Fig. 4A). It has been known for some time that a dense network of defect lines in a nematic LC displays considerable elasticity (*20*), but without permanent pinning centers, this elasticity decays in a matter of days. In our case, the percolated network pins the defects, and the elasticity lasts indefinitely (years).

Quantitatively, we find that the measured storage modulus for all particle sizes is given by

$$G'_{\max}(\phi) \approx G'_0 + \mathcal{G}(\phi - \phi_c)^{\nu} \qquad (1)$$

with the prefactor $\mathcal{G} \approx 10^5 \text{Pa} \approx K/l_c^2$ [when $K \sim 10^{-11}$ N (*21*)]. A full theory for this behavior is not yet available, but the relevant physics is reasonably clear. First, note that the form of the ϕ scaling is ubiquitous in percolated systems, which typically display a nonuniversal elasticity exponent in the range $1.5 \lesssim \nu \lesssim 3.5$ (*22*). Next, to understand the prefactor, we first recall that the elasticity of a network of defect lines with mesh size ξ can be estimated by K/ξ^2 (*23*). Thus, it appears that the scale of elasticity in our system $\mathcal{G}$ is set by defect lines packed at close to maximum possible density (one per l_c^2). We expect this to occur in the space between two particles entangled by disclinations (Fig. 4, B and C). A geometric argument (see SOM) then suggests that in a close packed system of defect-entangled particles ($\phi \approx 0.64$), the scale of the modulus is indeed set by $\sim K/l_c^2$, independent of particle size.

Finally, we turn to the kinetics of formation of our gel. Figure 2C shows that the recovery of the storage modulus is a two-staged process. Because our simulations show that this new form of soft matter is dominated by disclinations, we suggest that the kinetics of the initial, fast process are controlled by the relaxation of stretched disclination lines, which is dependent logarithmically on system size (*24*). Disclinations in a nematic LC with properties very similar to 5CB confined to $\sim 10^2$ μm, which is the order of magnitude of the gap size in our cone-plate rheometer, relax with a characteristic time of ~10 s (*24*), in good agreement with the location of the cross-over to a second process in our data (Fig. 2D). The latter is presumably due to the much slower relaxation of entangled disclination line in a disordered particle environment (*8*). It is known that the motion of defects in systems where they can be pinned into favorable metastable configurations by frozen-in disorder generically gives rise to kinetics with $\log(t)$ scaling (*25*). More interestingly, dynamics controlled by $\log(t)$ were also found in a model of a self-quenched glass (*26*).

Particles can also organize defects in 3D in other LC mesophases; for example, in a cholesteric, particles can act as nodes in a network of disclinations, even at $\phi \to 0$ (*23*). But in the nematic, which is the least ordered of all mesophases, we never observed isolated clusters linked by long defect lines in our simulations. Arrested states due to 3D entangled defects associated with particles in other mesophases remain to be discovered and characterized. Our entangled-defect colloidal gel (Fig. 1A) should also be carefully distinguished from the kind of foamlike soft solids previously made by quenching a dispersion of PMMA particles in the isotropic phase of 5CB to below T_{IN} (*17*). The latter relies on totally different physics: particles being jammed at (and therefore stabilizing) the interfaces between nematic domains, and a near analog being the "bijel" (*1*, *27*) (though the fact that the relevant order parameters are nonconserved and conserved, respectively, in LCs and binary liquids imposes interesting differences).

To summarize, we have dispersed hard-sphere colloids in thermotropic liquid crystals over a wide range of volume fractions. We find that beyond some critical volume fractions, $\phi_c \approx 12\%$, the elasticity of the samples increases rapidly, and the storage modulus exhibits power-law behavior $G' \sim (\phi - \phi_c)^{2.5}$. At high ϕ, the material yields at a strain of ~0.1%. Simulations suggest that we have prepared a defect-entangled gel in which the rigidity is due to a percolating network of disclination lines entangled with the particles.

Our material has conceptual similarities with vortex glasses in type II superconductors (*9*), where preexisting, static impurities pin vortex lines. Liquid crystals in random porous media (*8*) form a "soft matter analog" of such vortex glasses. However, in our case, the particles (pinning centers) generate the defects, and the collective motion of the defects and particles spontaneously organize each other into a jammed percolating network. Such a self-quenched glass of line defects, where the dynamical arrest does not originate from any intrinsic (quenched) disorder but arises from geometric constraints on the coupled motions of the interacting particle-disclination system (*28*), invites comparison with more traditional self-quenched glasses (*29*), especially structural

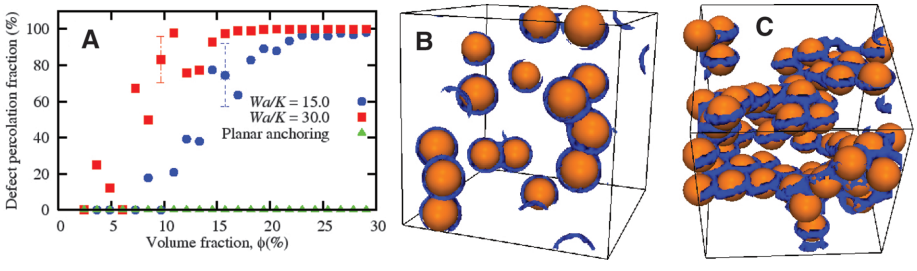

Fig. 4. (**A**) Fraction of percolated defects as a function of the colloid-packing fraction from simulations: weak homeotropic anchoring (blue circles), $Wa/K \approx 15$; strong homeotropic anchoring (red squares), $Wa/K \approx 30$; and planar anchoring (green triangles). The dotted lines denote a typical uncertainty (±SD). (**B**) Snapshot of a configuration with a nonpercolated defect line at $\phi = 4\%$. (**C**) Snapshot of a configuration with percolated defect lines at $\phi = 16\%$. In the snapshots, blue ribbons are defects, and oranges spheres are particles.

glasses of various kinds. Finally, we note that the very slow log(t) long-time aging of the storage modulus is reminiscent of similar stretched dynamics in systems with quenched (*9*) or self-induced (*26*, *28*) disorder.

References and Notes

1. E. M. Herzig, K. A. White, A. B. Schofield, W. C. K. Poon, P. S. Clegg, *Nat. Mater.* **6**, 966 (2007).
2. P. Poulin, H. Stark, T. C. Lubensky, D. A. Weitz, *Science* **275**, 1770 (1997).
3. U. Tkalec, M. Ravnik, S. Čopar, S. Žumer, I. Muševič, *Science* **333**, 62 (2011).
4. P. G. de Gennes, J. Prost, *The Physics of Liquid Crystals* (Oxford Univ. Press, Oxford, 1995).
5. S. K. Pal, A. Agarwal, N. L. Abbott, *Small* **5**, 2589 (2009).
6. A. Agarwal, E. Huang, S. Palecek, N. L. Abbott, *Adv. Mater.* **20**, 4804 (2008).
7. S. J. Woltman, G. D. Jay, G. P. Crawford, *Nat. Mater.* **6**, 929 (2007).
8. T. Araki, M. Buscaglia, T. Bellini, H. Tanaka, *Nat. Mater.* **10**, 303 (2011).
9. E. H. Brandt, *Rep. Prog. Phys.* **58**, 1465 (1995).
10. M. J. Bowick, L. Chandar, E. A. Schiff, A. M. Srivastava, *Science* **263**, 943 (1994).
11. H. Stark, *Phys. Rep.* **351**, 387 (2001).
12. R. W. Ruhwandl, E. M. Terentjev, *Phys. Rev. E* **55**, 2958 (1997).
13. I. Muševič, M. Škarabot, *Soft Matter* **4**, 195 (2008).
14. O. Guzmán, E. B. Kim, S. Grollau, N. L. Abbott, J. J. de Pablo, *Phys. Rev. Lett.* **91**, 235507 (2003).
15. T. Araki, H. Tanaka, *Phys. Rev. Lett.* **97**, 127801 (2006).
16. M. Ravnik *et al.*, *Phys. Rev. Lett.* **99**, 247801 (2007).
17. V. J. Anderson, E. M. Terentjev, S. P. Meeker, J. Crain, W. C. K. Poon, *Eur. Phys. J. E* **4**, 11 (2001).
18. A. G. Chmielewski, E. Lepakiewicz, *Rheol. Acta* **23**, 207 (1984).
19. A. Mertelj, M. Čopič, *Phys. Rev. E* **69**, 021711 (2004).
20. L. M. Walker, N. J. Wagner, R. G. Larson, P. A. Mirau, P. Moldenaers, *J. Rheol.* **39**, 925 (1995).
21. J. D. Bunning, T. E. Faber, P. L. Sherrell, *J. Phys.* **42**, 1175 (1981).
22. L. Benguigui, *Phys. Rev. Lett.* **53**, 2028 (1984).
23. M. Zapotocky, L. Ramos, P. Poulin, T. C. Lubensky, D. A. Weitz, *Science* **283**, 209 (1999).
24. N. Osterman, J. Kotar, E. M. Terentjev, P. Cicuta, *Phys. Rev. E* **81**, 061701 (2010).
25. A. J. Bray, *Adv. Phys.* **43**, 357 (1994).
26. J. Török, S. Krishnamurthy, J. Kertész, S. Roux, *Eur. Phys. J. B* **18**, 697 (2000).
27. K. Stratford, R. Adhikari, I. Pagonabarraga, J.-C. Desplat, M. E. Cates, *Science* **309**, 2198 (2005).
28. L. F. Cugliandolo, J. Kurchan, R. Monasson, G. Parisi, *J. Phys. A* **29**, 1347 (1996).
29. L. Berthier, G. Biroli, *Rev. Mod. Phys.* **83**, 587 (2011).

Acknowledgments: The work was funded by Engineering and Physical Sciences Research Council grants EP/D071070/1 and EP/E030173/1. We thank R. Besseling and M. Cates for illuminating discussions.

Supporting Online Material

www.sciencemag.org/cgi/content/full/334/6052/79/DC1
Materials and Methods
SOM Text
Figs. S1 to S4
References (*30*–*38*)

17 June 2011; accepted 24 August 2011
10.1126/science.1209997

Adaptation to Climate Across the *Arabidopsis thaliana* Genome

Angela M. Hancock,[1] Benjamin Brachi,[2] Nathalie Faure,[2] Matthew W. Horton,[1] Lucien B. Jarymowycz,[1] F. Gianluca Sperone,[1] Chris Toomajian,[3] Fabrice Roux,[2] Joy Bergelson[1]*

Understanding the genetic bases and modes of adaptation to current climatic conditions is essential to accurately predict responses to future environmental change. We conducted a genome-wide scan to identify climate-adaptive genetic loci and pathways in the plant *Arabidopsis thaliana*. Amino acid–changing variants were significantly enriched among the loci strongly correlated with climate, suggesting that our scan effectively detects adaptive alleles. Moreover, from our results, we successfully predicted relative fitness among a set of geographically diverse *A. thaliana* accessions when grown together in a common environment. Our results provide a set of candidates for dissecting the molecular bases of climate adaptations, as well as insights about the prevalence of selective sweeps, which has implications for predicting the rate of adaptation.

Climate change has already led to altered distributions of species, phenotypic variation, and allele frequencies (*1*–*5*), and the impact of changing climates is expected to intensify. The capacity to respond to changing climate is likely to vary widely as a consequence of variation among species in their degree of phenotypic plasticity and their potential for genetic adaptation (*6*), which in turn depends on the amount of standing genetic variation and the rate at which new genetic variation arises. *Arabidopsis thaliana* is an excellent model for investigating the genetic basis and mode of adaptation to climate owing to the extensive climatic variation across its native range, as well as the availability of genome-wide single-nucleotide polymorphism (SNP) data among a geographically diverse collection. We examined the correlations between 107 ecologically important phenotypes in *A. thaliana* (*7*) and 13 climate variables that represent extremes and seasonality of temperature and precipitation, photosynthetically active radiation (PAR), relative humidity, season lengths, and aridity (figs. S1 to S4). We observed strong correlations between

[1]Department of Ecology and Evolution, University of Chicago, 1101 East 57th Street, Chicago, IL 60637, USA. [2]Laboratoire Génétique et Evolution des Populations Végétales, FRE CNRS 3268, Université des Sciences et Technologies de Lille 1, Villeneuve d'Ascq, France. [3]Department of Plant Pathology, Kansas State University, Manhattan, KS 66502, USA.

*To whom correspondence should be addressed. E-mail: jbergels@uchicago.edu

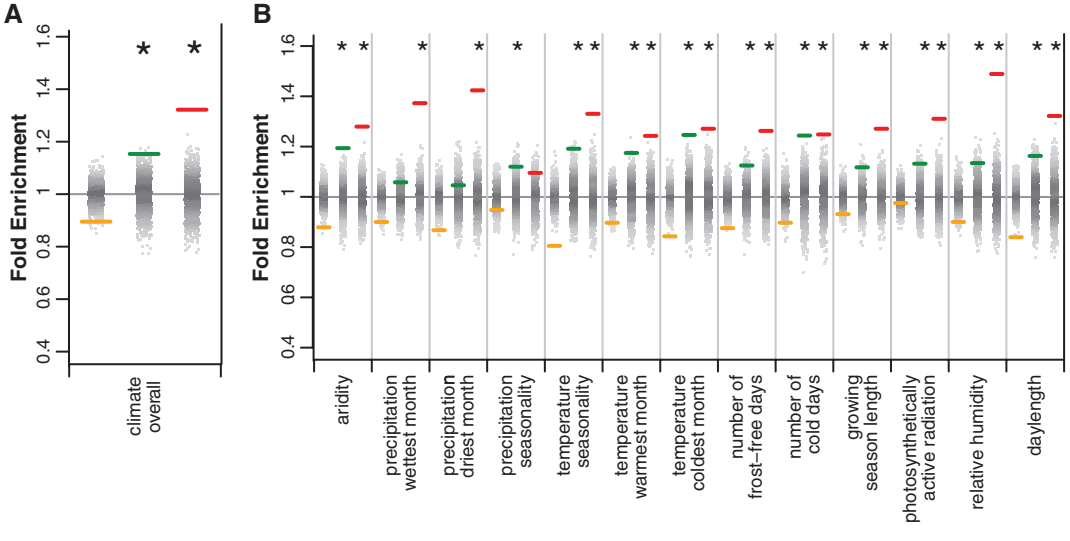

Fig. 1. Enrichment of amino acid–changing SNPs (red), synonymous SNPs (green), and intergenic SNPs (yellow) in the 1% tails of the distributions for (**A**) climate overall (using a rank statistic based on the minimum rank across climate variables) and (**B**) for each individual climate variable. Enrichments shown are relative to the proportion of each class of SNPs in the genome overall. Gray dots show the distribution of results of 1000 permutations. The gray line shows the expected enrichment under the null hypothesis of no enrichment. Enrichments that are significant relative to permutations are denoted by asterisks.